Integrating the best-fit SED of GNz7q through the Pan-STARRS1 z and UKIRT y and J filter bandpasses, we find it has $z - y = 5.8$ and $y - J = 0.5$, which comfortably satisfies the optical–NIR quasar selection criterion. This indicates that the quasar population similar to GNz7q could be identified in previous high-z quasar surveys if the data are sufficiently deep, such as The Canada–France High-z Quasar Survey[165] and Subaru High-z Exploration of Low-luminosity Quasars[51–53,55]. GNz7q also meets the optical–NIR colour criteria used in recent discoveries of the luminous quasars at $z \sim 7.5$[4,6,49], although the optical–NIR data of the wide-area surveys used in these discoveries is almost 2 orders magnitude shallower than that of the GOODS-North field. These colour selection results indicate that the identification of GNz7q at $z = 7.2$ in the relatively small area of the entire *HST* archive might be just explained by chance, although the expected probability is less than 1% from the quasar luminosity function[26] and the red quasar fraction at $z \sim 6$.[25] There are two other possibilities. The first is that the transitioning young quasar more frequently emerges at $z > 7$ than at $z = 6$. The second is that the quasar population similar to GNz7q has been identified in the previous surveys, but not regarded or classified as a quasar due to its faintness in the rest-frame UV, MIR, X-ray, and radio continuum in the follow-up spectroscopy and/or multi-wavelength analyses. In fact, the presence of the deep *HST* and MIPS data is crucial for the interpretation for GNz7q (Section 5). Without them, the uniquely-faint properties of GNz7q in the rest-frame UV emission lines and X-ray generally conclude its classification as a luminous galaxy. Recent studies have also suggested, both observationally and theoretically, a potential high abundance of the dust-rich quasar population at $z > 7$[28,170]. A systematic deep, high-resolution optical–MIR imaging campaign for all luminous high-z galaxy candidates could lead to additional discoveries similar to GNz7q. Given the relatively robust calibration[166] and lesser effects from the slim disk, detecting broad Balmer emission lines could provide a decisive conclusion for the quasar classification, which will soon become possible even at $z > 7$ with the launch of the *James Webb Space Telescope*. Moreover, even if we do not detect the broad lines with *JWST*, the results will suggest further exciting possibilities: the existence of an extraordinary UV luminous and compact star-forming region (Extended Data Fig. 7), or that is exactly what the first quasars look like.

Code availability. The *HST* and *Spitzer* data were processed with GRIZLI and GOLFIR, available at `https://github.com/gbrammer/grizli` and `https://github.com/gbrammer/golfir`, respectively. The *HST* F125W image is analyzed with GALFIT which is available at `https://users.obs.carnegiescience.edu/peng/work/galfit/galfit.html`. The NOEMA data were reduced using the GILDAS software. The CASA pipeline version of 5.6 is also used for imaging the NOEMA interferometric data. These are available at `https://casa.nrao.edu/casa_obtaining.shtml`. `https://www.oso.nordic-alma.se/software-tools.php`. The online Portable Interactive Multi-Mission Simulator is available at `https://heasarc.gsfc.nasa.gov/cgi-bin/Tools/w3pimms/w3pimms.pl`.

Data availability. This paper makes use of the following *HST* data from programs 9583, 9727, 9728, 10189, 10339, 11600, 12442, 12443, 12444, 12445, 13063, 13420, 13779, available at `https://archive.stsci.edu/`. The reduced *HST* and *Spitzer* image mosaics are available at `https://doi.org/10.5281/zenodo.4469734`. Other products from the CHArGE

project are avilable at https://gbrammer.github.io/projects/charge/. The NOEMA data that supports our finding consists of ED19AD and W20EO that are available at https://www.iram-institute.org/EN/content-page-386-7-386-0-0-0.html. The SED of the SDSS quasar at $z = 3.11$ used in Fig. 1 is available from the SDSS DR12 website https://dr12.sdss.org/spectrumDetail?plateid=6839&mjd=56425&fiber=146. The SEDs of local quasar and starburst are available from the SWIRE template website http://www.iasf-milano.inaf.it/$\sim$polletta/templates/swire_templates.html. The datasets generated and/or analyzed during the current study are available from the corresponding author on reasonable request.

30. Planck Collaboration. Planck 2013 results. XVI. Cosmological parameters. *Astronomy & Astrophysics* **571**, A16 (2014).

31. Onoue, M. et al. Subaru High-z Exploration of Low-luminosity Quasars (SHELLQs). XIV. A Candidate Type II Quasar at $z = 6.1292$ *Astrophysical Journal* **919**, 1 (2021)

32. Antonucci, R. Unified Models for Active Galactic Nuclei and Quasars *Annual Review of Astronomy and Astrophysics* **31**, 473–521 (1993)

33. Urry, C. and Padovani, P. Unified Schemes for Radio-Loud Active Galactic Nuclei *Publications of the Astronomical Society of the Pacific* **107**, 803 (1995)

34. Richards et al. Red and Reddened Quasars in the Sloan Digital Sky Survey *The Astronomical Journal* **126**, 3, 1131–1147 (2003)

35. Ross, N. et al. Extremely red quasars from SDSS, BOSS and WISE: classification of optical spectra *Monthly Notices of the Royal Astronomical Society* **453**, 4, 3932–3952 (2015)

36. Hamann, F. et al. Extremely red quasars in BOSS *Monthly Notices of the Royal Astronomical Society* **464**, 3, 3431–3463 (2017)

37. Glikman, E. et al. FIRST-2Mass Sources below the APM Detection Threshold: A Population of Highly Reddened Quasars *Astrophysical Journal* **607**, 1 (2004)

38. Urrutia, T. et al. The FIRST-2MASS Red Quasar Survey. II. An Anomalously High Fraction of LoBALs in Searches for Dust-Reddened Quasars *Astrophysical Journal* **698**, 2 (2009)

39. Lacy, M. et al. Optical Spectroscopy and X-Ray Detections of a Sample of Quasars and Active Galactic Nuclei Selected in the Mid-Infrared from Two Spitzer Space Telescope Wide-Area Surveys *The Astronomical Journal* **133**, 1, (2007)

40. Glikman, E. et al. Dust Reddened Quasars in FIRST and UKIDSS: Beyond the Tip of the Iceberg *Astrophysical Journal* **778**, 2, 186–205 (2013)

41. Krawczyk, C. et al. Mining for Dust in Type 1 Quasars *Astrophysical Journal* **149**, 6 (2015)

42. Díaz-santos, T. et al. The multiple merger assembly of a hyperluminous obscured quasar at redshift 4.6 *Science* **362**, 6418, L17 (2018)

43. Díaz-santos, T. et al. Kinematics and Star Formation of High-Redshift Hot Dust-Obscured Quasars as Seen by ALMA *Astronomy & Astrophysics* **654**, A37 (2021)

44. Finnerty, L. et al. Fast Outflows in Hot Dust-obscured Galaxies Detected with Keck/NIRES *Astrophysical Journal* **905**, 1 (2020)

45. Alexander, M. et al. Weighing the Black Holes in $z \sim 2$ Submillimeter-Emitting Galaxies Hosting Active Galactic Nuclei *The Astronomical Journal* **135**, 5, 1968–1981 (2008)

46. GAIA Collaboration Gaia Data Release 2. Summary of the contents and survey properties *Astronomy & Astrophysics* **616**, A1 (2018)

47. Brammer, G. Grizli: grism redshift and line analysis software *Astrophysics Source Code Library*. ascl:1905.001 (2019) (2019)

48. Shindler, J. et al. The X-SHOOTER/ALMA Sample of Quasars in the Epoch of Reionization. I. NIR Spectral Modeling, Iron Enrichment, and Broad Emission Line Properties *Astrophysical Journal* **905**, 1, (2020)

49. Yang, J. et al. Pōniuā'ena: A Luminous $z = 7.5$ Quasar Hosting a 1.5 Billion Solar Mass Black Hole *Astrophysical Journal Letter* **897**, 1, L14 (2020).

50. Bowler, R. et al. Unveiling the nature of bright $z \simeq 7$ galaxies with the Hubble Space Telescope *Monthly Notices of the Royal Astronomical Society* **466**, 3612–3635 (2017)

51. Matsuoka, Y. et al. Subaru High-z Exploration of Low-luminosity Quasars (SHELLQs). I. Discovery of 15 Quasars and Bright Galaxies at $5.7 \lesssim z \lesssim 6.9$ *Astrophysical Journal* **828**, 1 (2016)

52. Matsuoka, Y. et al. Subaru High-z Exploration of Low-Luminosity Quasars (SHELLQs). II. Discovery of 32 quasars and luminous galaxies at $5.7 < z \leq 6.8$ *Publications of the Astronomical Society of Japan* **70**, S35 (2017)

53. Matsuoka, Y. et al. Subaru High-z Exploration of Low-luminosity Quasars (SHELLQs). IV. Discovery of 41 Quasars and Luminous Galaxies at $5.7 \leq z \leq 6.9$ *Astrophysical Journal Supplement Series* **237**, 5, (2018)

54. Matsuoka, Y. et al. Discovery of the First Low-luminosity Quasar at $z \geq 7$ *Astrophysical Journal Letters* **872**, L1 (2019)

55. Matsuoka, Y. et al. Subaru High-z Exploration of Low-luminosity Quasars (SHELLQs). X. Discovery of 35 Quasars and Luminous Galaxies at $5.7 \leq z \leq 7.0$ *Astrophysical Journal* **883**, 2 (2019)

56. Onoue, M. et al. Subaru High-z Exploration of Low-luminosity Quasars (SHELLQs). VI. Black Hole Mass Measurements of Six Quasars at 6.1 $\leq z \leq$6.7 *Astrophysical Journal* **880**, 2 (2019)

57. Schouws, S. et al. Significant Dust-Obscured Star Formation in Luminous Lyman-break Galaxies at $z \sim 7-8$ *Astrophysical Journal* in press, (2021) (arXiv:2105.12133)

58. Peng, C. Y. et al. Detailed Decomposition of Galaxy Images. II. Beyond Axisymmetric Models *The Astronomical Journal* **139**, 2097–2129 (2010)

59. McMullin, J. et al. CASA Architecture and Applications *Astronomical Data Analysis Software and Systems XVI* **376**, 127 (2007)

60. Martí-Vidal, I. et al. Over-resolution of compact sources in interferometric observations *Astronomy & Astrophysics* **541**, A135 (2012)

61. Fujimoto, S. et al. Demonstrating A New Census of INfrared Galaxies with ALMA (DANCING-ALMA). I. FIR Size and Luminosity Relation at $z = 0-6$ Revealed with 1034 ALMA Sources *Astrophysical Journal* **850**, 1 (2017)

62. Franco, M. et al. GOODS-ALMA: 1.1 mm galaxy survey. I. Source catalog and optically dark galaxies *Astronomy & Astrophysics* **620**, A152 (2018)

63. Franco, M. et al. GOODS-ALMA: The slow downfall of star formation in z = 2-3 massive galaxies *Astronomy & Astrophysics* **643**, A30 (2020)

64. Wang, T. et al. A dominant population of optically invisible massive galaxies in the early Universe *Nature* **572**, 7768, 211–214 (2019)

65. Fudamoto, Y. et al. Normal, dust-obscured galaxies in the epoch of reionization *Nature* **597**, 7877, 489-492 (2021)

66. Cortzen, I. et al. Deceptively cold dust in the massive starburst galaxy GN20 at $z \sim 4$ *Astronomy & Astrophysics* **634**, L14 (2007)

67. Jin, S. et al. Discovery of Four Apparently Cold Dusty Galaxies at $z = 3.62-5.85$ in the COSMOS Field: Direct Evidence of Cosmic Microwave Background Impact on High-redshift Galaxy Observables *Astrophysical Journal* **887**, 2 (2019)

68. Da Cunha, E. et al. An ALMA Survey of Sub-millimeter Galaxies in the Extended Chandra Deep Field South: Physical Properties Derived from Ultraviolet-to-radio Modeling *Astrophysical Journal* **806**, 110 (2015)

69. Kajisawa et al. MOIRCS Deep Survey. IX. Deep Near-Infrared Imaging Data and Source Catalog *Publications of the Astronomical Society of Japan* **63**, 379 (2011)

70. Magnelli et al. Evolution of the dusty infrared luminosity function from $z = 0$ to $z = 2.3$ using observations from Spitzer *Astronomy & Astrophysics* **528**, 35 (2011)

71. Cowie, L. et al. A Submillimeter Perspective on the GOODS Fields (SUPER GOODS). I. An Ultradeep SCUBA-2 Survey of the GOODS-N *Astrophysical Journal* **837**, 2, 139 (2017)

72. Owen, F. Deep JVLA Imaging of GOODS-N at 20 cm *Astrophysical Journal Supplements Series* **235**, 2 (2018)

73. Liu, D. et al. Super-deblended Dust Emission in Galaxies. I. The GOODS-North Catalog and the Cosmic Star Formation Rate Density out to Redshift 6 *Astrophysical Journal* **853**, 172 (2018)

74. Oliver, S. et al. The Herschel Multi-tiered Extragalactic Survey: HerMES *Monthly Notices of the Royal Astronomical Society* **424**, 1614–1645 (2018)

75. Murphy, E. et al. The GOODS-N Jansky VLA 10-GHz Pilot Survey: Sizes of Star-forming μJY Radio Sources *Astrophysical Journal* **839**, 1 (2017)

76. Geach, J. et al. The SCUBA-2 Cosmology Legacy Survey: 850 μm maps, catalogues and number counts *Monthly Notices of the Royal Astronomical Society* **465**, 1789–1806 (2017)

77. Nanni, R. et al. The X-ray properties of $z \sim 6$ luminous quasars *Astronomy & Astrophysics* **603**, A128 (2017)

78. Vito, F. et al. Heavy X-ray obscuration in the most luminous galaxies discovered by WISE *Monthly Notices of the Royal Astronomical Society* **474**, 4, 4528–4540 (2018)

79. HI4PI Collaboration. HI4PI: A full-sky H I survey based on EBHIS and GASS *Astronomy & Astrophysics* **594**, A116 (2016)

80. Wang, F. et al. Revealing the Accretion Physics of Supermassive Black Holes at Redshift $z \sim 7$ with Chandra and Infrared Observations *Astrophysical Journal* **908**, 1 (2021)

81. Lusso, E. et al. The Tight Relation between X-Ray and Ultraviolet Luminosity of Quasars *Astrophysical Journal* **819**, 2 (2016)

82. Vito, F. et al. The X-ray properties of $z > 6$ quasars: no evident evolution of accretion physics in the first Gyr of the Universe *Astronomy & Astrophysics* **630**, A118 (2019)

83. Chiaraluce, E. et al. The X-ray/UV ratio in active galactic nuclei: dispersion and variability *Astronomy & Astrophysics* **619**, A95 (2018)

84. Zou, F. et al. X-ray properties of dust-obscured galaxies with broad optical/UV emission lines *Monthly Notices of the Royal Astronomical Society* **499**, 2, 1823–1840 (2020)

85. Shemmer, O. et al. Chandra Observations of the Highest Redshift Quasars from the Sloan Digital Sky Survey *Astrophysical Journal* **644**, 1 (2006)

86. Kim, Y. et al. High Star Formation Rates of Low Eddington Ratio Quasars at $z \gtrsim 6$ *Astrophysical Journal* **879**, 2 (2019)

87. Iwasawa, K. et al. C-GOALS: Chandra observations of a complete sample of luminous infrared galaxies from the IRAS Revised Bright Galaxy Survey *Astronomy & Astrophysics* **529**, A106 (2011)

88. Veilleux, B. et al. A Deep Hubble Space Telescope H-Band Imaging Survey of Massive Gas-Rich Mergers. II. The QUEST QSOs *Astrophysical Journal* **701**, 1 (2009)

89. Ni, Q. et al. Connecting the X-ray properties of weak-line and typical quasars: testing for a geometrically thick accretion disk *Monthly Notices of the Royal Astronomical Society* **480**, 4, 5184–5202 (2018)

90. Marques-Chaves, R. et al. The discovery of the most UV-Lyα luminous star-forming galaxy: a young, dust- and metal-poor starburst with QSO-like luminosities *Monthly Notices of the Royal Astronomical Society* **499**, 1 (2020)

91. Shibuya, T. et al. Morphologies of $\sim 190,000$ Galaxies at $z = 0 - 10$ Revealed with HST Legacy Data. I. Size Evolution *Astrophysical Journal Supplement Series* **219**, 15 (2019)

92. Conroy, C. et al. The Propagation of Uncertainties in Stellar Population Synthesis Modeling. I. The Relevance of Uncertain Aspects of Stellar Evolution and the Initial Mass Function to the Derived Physical Properties of Galaxies *Astrophysical Journal* **699**, 486 (2009)

93. Conroy, C. & Gunn, J. The Propagation of Uncertainties in Stellar Population Synthesis Modeling. III. Model Calibration, Comparison, and Evaluation *Astrophysical Journal* **712**, 833 (2010)

94. Brammer, G. et al. EAZY: A Fast, Public Photometric Redshift Code *Astrophysical Journal* **686**, 2 (2008)

95. Polletta, M. et al. Spectral Energy Distributions of Hard X-Ray Selected Active Galactic Nuclei in the XMM-Newton Medium Deep Survey *Astrophysical Journal* **663**, 1 (2007)

96. Glikman, E. et al. A Near-Infrared Spectral Template for Quasars *Astrophysical Journal* **640**, 2 (2006)

97. Leipski, C. et al. Spectral Energy Distributions of QSOs at $z > 5$: Common Active Galactic Nucleus-heated Dust and Occasionally Strong Star-formation *Astrophysical Journal* **785**, 2 (2014)

98. Nenkova, M. et al. AGN Dusty Tori. I. Handling of Clumpy Media *Astrophysical Journal* **685**, 147 (2008)

99. Leja, J. et al. Hot Dust in Panchromatic SED Fitting: Identification of Active Galactic Nuclei and Improved Galaxy Properties *Astrophysical Journal* **854**, 62 (2018)

100. Diamond-Stanic, A. et al. High-redshift SDSS Quasars with Weak Emission Lines *Astrophysical Journal* **699**, 1 (2009)

101. Andika, I. et al. Probing the Nature of High-redshift Weak Emission Line Quasars: A Young Quasar with a Starburst Host Galaxy *Astrophysical Journal* **903**, 1 (2020)

102. Wu, J. et al. X-Ray and Multiwavelength Insights into the Nature of Weak Emission-line Quasars at Low Redshift *Astrophysical Journal* **747**, 1 (2012)

103. Vito, F. et al. Chandra and Magellan/FIRE follow-up observations of PSO167-13: An X-ray weak QSO at $z = 6.515$ *Astronomy & Astrophysics* **649**, A133 (2021)

104. Gallagher, S. C. et al. X-Raying the Ultraluminous Infrared Starburst Galaxy and Broad Absorption Line QSO Markarian 231 with Chandra *Astrophysical Journal* **569**, 655 (2002)

105. Braito, V. et al. The XMM-Newton and BeppoSAX view of the Ultra Luminous Infrared Galaxy MKN 231 *Astronomy & Astrophysics* **420**, 79 (2004)

106. Lipari, S., Colina, L., and Macchetto, F. Galaxies with Extreme Infrared and Fe II Emission. I. Markarian 231: The Signature of a Young Infrared QSO *Astronomy & Astrophysics* **427**, 174L (1994)

107. Veilleux, S. et al. The Complete Ultraviolet Spectrum of the Archetypal "Wind-dominated" Quasar Mrk 231: Absorption and Emission from a High-speed Dusty Nuclear Outflow *Astrophysical Journal* **825**, 42 (2016)

108. Kokorev, V. et al. The Evolving Interstellar Medium of Star-Forming Galaxies, as traced by `Stardust` *Astrophysical Journal* **921**, 1 (2021)

109. Draine, B. and Li, A. Infrared Emission from Interstellar Dust. IV. The Silicate-Graphite-PAH Model in the Post-Spitzer Era *Astrophysical Journal* **657**, 2 (2007)

110. Mullaney, J. et al. GOODS-Herschel: the far-infrared view of star formation in active galactic nucleus host galaxies since $z \approx 3$ *Monthly Notices of the Royal Astronomical Society* **419**, 1, 95–115 (2012)

111. Shen, Y. et al. The Sloan Digital Sky Survey Reverberation Mapping Project: Velocity Shifts of Quasar Emission Lines *Astrophysical Journal* **831**, 1 (2016)

112. Murphy, E. et al. Calibrating Extinction-free Star Formation Rate Diagnostics with 33 GHz Free-free Emission in NGC 6946 *Astrophysical Journal* **737**, 67 (2011)

113. Kroupa, P. On the variation of the initial mass function *Monthly Notices of the Royal Astronomical Society* **322**, 2, 231–246 (2001)

114. Simpson, J. et al. The SCUBA-2 Cosmology Legacy Survey: ALMA Resolves the Rest-frame Far-infrared Emission of Sub-millimeter Galaxies *Astrophysical Journal* **799**, 81 (2015)

115. Lehmer, B. et al. The Evolution of Normal Galaxy X-Ray Emission through Cosmic History: Constraints from the 6 MS Chandra Deep Field-South *Astrophysical Journal* **825**, 1 (2016)

116. Fornasini, F. et al. The MOSDEF Survey: The Metallicity Dependence of X-Ray Binary Populations at $z \sim 2$ *Astrophysical Journal* **885**, 1 (2019)

117. Fornasini, F. et al. Connecting the metallicity dependence and redshift evolution of high-mass X-ray binaries *Monthly Notices of the Royal Astronomical Society* **495**, 1, 771-783 (2020)

118. Novak, M. et al. An ALMA Multiline Survey of the Interstellar Medium of the Redshift 7.5 Quasar Host Galaxy J1342+0928 *Astrophysical Journal* **881**, 1 (2019)

119. Magdis, G. et al. The Evolving Interstellar Medium of Star-forming Galaxies since z = 2 as Probed by Their Infrared Spectral Energy Distributions *Astrophysical Journal* **760**, 1 (2012)

120. Scoville, N. et al. ISM Masses and the Star formation Law at $z = 1$ to 6: ALMA Observations of Dust Continuum in 145 Galaxies in the COSMOS Survey Field *Astrophysical Journal* **820**, 2 (2016)

121. Solmon, P. et al. Mass, Luminosity, and Line Width Relations of Galactic Molecular Clouds *Astrophysical Journal* **319**, 730 (1987)

122. Zanella, A. et al. The [C II] emission as a molecular gas mass tracer in galaxies at low and high redshifts *Monthly Notices of the Royal Astronomical Society* **481**, 2, 1976–1999 (2018)

123. Riechers, D. et al. A dust-obscured massive maximum-starburst galaxy at a redshift of 6.34 *Nature* **496**, 329–333 (2013)

124. Strandet, M. et al. ISM Properties of a Massive Dusty Star-forming Galaxy Discovered at $z \sim 7$ *Astrophysical Journal Letter* **842**, 2, L15 (2017)

125. Crocker, A. et al. [C I](1–0) and [C I](2–1) in Resolved Local Galaxies *Astrophysical Journal* **887**, 1 (2019)

126. Valentino, F. et al. A Survey of Atomic Carbon [C I] in High-redshift Main-sequence Galaxies *Astrophysical Journal* **869**, 1 (2018)

127. Bothwell, S. et al. A survey of molecular gas in luminous sub-millimetre galaxies *Monthly Notices of the Royal Astronomical Society* **429**, 4, 3047–3067 (2013)

128. Wang, R. et al. Star Formation and Gas Kinematics of Quasar Host Galaxies at $z \sim 6$: New Insights from ALMA *Astrophysical Journal* **773**, 44 (2013)

129. Decarli, R. et al. An ALMA [C II] Survey of 27 Quasars at $z \gtrsim 5.94$ *Astrophysical Journal* **854**, 97 (2018)

130. Izumi, T. et al. Subaru High-z Exploration of Low-Luminosity Quasars (SHELLQs). III. Star formation properties of the host galaxies at $z \gtrsim 6$ studied with ALMA *Publications of the Astronomical Society of Japan* **70**, 3 (2018)

131. Di Teodoro, T. et al. Spitzer Observations of Young Red Quasars *Astrophysical Journal* **757**, 2 (2012)

132. Zakamska, N. et al. Discovery of extreme [O III] λ5007 A outflows in high-redshift red quasars *Monthly Notices of the Royal Astronomical Society* **459**, 3, 3144–3160 (2016)

133. Bongiorno, A. et al. The $M_{\rm BH}$-$M_\star$ relation for X-ray-obscured, red QSOs at $1.2 < z < 2.6$ *Monthly Notices of the Royal Astronomical Society* **443**, 3, 2077–2091 (2014)

134. Díaz-Santos, T. et al. Explaining the [C II] 157.7 μm Deficit in Luminous Infrared Galaxies—First Results from a Herschel/PACS Study of the GOALS Sample *Astrophysical Journal* **774**, 1 (2013)

135. Spilker, J. et al. ALMA Imaging and Gravitational Lens Models of South Pole Telescope – Selected Dusty, Star-Forming Galaxies at High Redshifts *Astrophysical Journal* **826**, 2 (2016)

136. Gullberg, B. et al. The Dust and [C II] Morphologies of Redshift $\sim$4.5 Sub-millimeter Galaxies at $\sim$ 200 pc Resolution: The Absence of Large Clumps in the Interstellar Medium at High-redshift *Astrophysical Journal* **859**, 1 (2018)

137. Laporte, N. et al. Dust in the Reionization Era: ALMA Observations of a z = 8.38 Gravitationally Lensed Galaxy *Astrophysical Journal Letter* **837**, L21 (2017)

138. Hashimoto, T. et al. Big Three Dragons: A $z = 7.15$ Lyman-break galaxy detected [O III] 88 μm, [C II] 158 μm, and dust continuum with ALMA *Publications of the Astronomical Society of Japan* **71**, 4 (2019)

139. Bakx, T. et al. ALMA uncovers the [C II] emission and warm dust continuum in a $z = 8.31$ Lyman break galaxy *Monthly Notices of the Royal Astronomical Society* **493**, 3, 4294–4307 (2020)

140. Izumi, T. et al. Subaru High-z Exploration of Low-luminosity Quasars (SHELLQs). XII. Extended [C II] Structure (Merger or Outflow) in a z = 6.72 Red Quasar *Astrophysical Journal* **908**, 2 (2021)

141. Fan, L. et al. The Spectral Energy Distribution of the Hyperluminous, Hot Dust-obscured Galaxy W2246-0526 *Astrophysical Journal* **854**, 2 (2018)

142. Venemans, B. et al. Kiloparsec-scale ALMA Imaging of [C II] and Dust Continuum Emission of 27 Quasar Host Galaxies at $z \sim 6$ *Astrophysical Journal* **904**, 2 (130)

143. Hashimoto, T. et al. Detections of [O III] 88 μm in two quasars in the reionization epoch *Publications of the Astronomical Society of Japan* **71**, 6 (2019)

144. Walter, F. et al. No Evidence for Enhanced [O III] 88 μm Emission in a $z \sim 6$ Quasar Compared to Its Companion Starbursting Galaxy *Astrophysical Journal Letters* **869**, L22 (2018)

145. Harikane, Y. et al. Large Population of ALMA Galaxies at $z > 6$ with Very High [O III] 88 μm to [C II] 158 μm Flux Ratios: Evidence of Extremely High Ionization Parameter or PDR Deficit? *Astrophysical Journal* **896**, 2 (2020)

146. Pensabene, A. et al. The ALMA view of the high-redshift relation between supermassive black holes and their host galaxies *Astronomy & Astrophysics* **637**, A84 (2020)

147. Neeleman, M. et al. The Kinematics of $z\tilde{6}$ Quasar Host Galaxies *Astrophysical Journal* **911**, 141

148. Willott, C. et al. Star Formation Rate and Dynamical Mass of 10^8 Solar Mass Black Hole Host Galaxies At Redshift 6 *Astrophysical Journal* **801**, 2 (2015)

149. Willott, C. et al. A Wide Dispersion in Star Formation Rate and Dynamical Mass of 10^8 Solar Mass Black Hole Host Galaxies at Redshift 6 *Astrophysical Journal* **850**, 108 (2017)

150. Venemans, B. et al. The Compact, $\simeq$ 1 kpc Host Galaxy of a Quasar at a Redshift of 7.1 *Astrophysical Journal* **837**, 146 (2017)

151. Izumi, T. et al. Subaru High-z Exploration of Low-Luminosity Quasars (SHELLQs). VIII. A less biased view of the early co-evolution of black holes and host galaxies *Publications of the Astronomical Society of Japan* **71**, 6 (2019)

152. Kormendy, J. & Ho, L. Coevolution (Or Not) of Supermassive Black Holes and Host Galaxies *Annual Review of Astronomy and Astrophysics* **51**, 1, 511–653 (2013)

153. Reines, A. et al. Relations between Central Black Hole Mass and Total Galaxy Stellar Mass in the Local Universe *Astrophysical Journal* **813**, 2 (2015)

154. Ibar, E. et al. Deep multi-frequency radio imaging in the Lockman Hole - II. The spectral index of submillimetre galaxies *Monthly Notices of the Royal Astronomical Society* **401**, 1, L53-L57 (2010)

155. Yun, M. et al. Radio Properties of Infrared-selected Galaxies in the IRAS 2 Jy Sample *Astrophysical Journal* **554**, 2 (2001)

156. Magnelli, B. et al. Far-infrared properties of submillimeter and optically faint radio galaxies *Astronomy & Astrophysics* **518**, L28 (2010)

157. Delhaize, J. et al. The VLA-COSMOS 3 GHz Large Project: The infrared-radio correlation of star-forming galaxies and AGN to $z \lesssim 6$ *Astronomy & Astrophysics* **602**, A4 (2017)

158. Dunlop, J. et al. Quasars, their host galaxies and their central black holes *Monthly Notices of the Royal Astronomical Society* **401**, 1, 1095–1135 (2003)

159. Valiante, R. et al. The origin of the dust in high-redshift quasars: the case of SDSS J1148+5251 *Monthly Notices of the Royal Astronomical Society* **416**, 3, 1916–1935 (2011)

160. Valiante, R. et al. High-redshift quasars host galaxies: is there a stellar mass crisis? *Monthly Notices of the Royal Astronomical Society* **444**, 3, 2442–2455 (2014)

161. Pezzulli, E. et al. Faint progenitors of luminous $z{\sim}6$ quasars: Why do not we see them? *Monthly Notices of the Royal Astronomical Society* **466**, 2, 2131–2142 (2017)

162. Mazzucchelli, C. et al. Physical Properties of 15 Quasars at $z \gtrsim 6.5$ *Astrophysical Journal* **849**, 2 (2017)

163. Morganson, E. et al. The First High-redshift Quasar from Pan-STARRS *The Astronomical Journal* **143**, 6 (2012)

164. Lawrence, A. et al. The UKIRT Infrared Deep Sky Survey (UKIDSS) *Monthly Notices of the Royal Astronomical Society* **379**, 4, 1599-1617 (2007)

165. Willott, C. et al. The Canada-France High-z Quasar Survey: Nine New Quasars and the Luminosity Function at Redshift 6 *The Astronomical Journal* **139**, 3, 906-918 (2010)

166. Vestergaard, M. & Peterson, B. M. Determining Central Black Hole Masses in Distant Active Galaxies and Quasars. II. Improved Optical and UV Scaling Relationships *Astrophysical Journal* **641**, 689 (2006)

167. Anderson, J. Empirical Models for the WFC3/IR PSF *Space Telescope WFC Instrument Science Report* **12** (2016)

168. Just, D. et al. The X-Ray Properties of the Most Luminous Quasars from the Sloan Digital Sky Survey *Astrophysical Journal* **665**, 2 (2007)

169. Sargsyan, L. et al. [C II] 158 μmLuminosities and Star Formation Rate in Dusty Starbursts and Active Galactic Nuclei *Astrophysical Journal* **755**, 2 (2012)

170. Davies, F. B., Hennawi, J. F., & Eilers, A.-C. Evidence for low radiative efficiency or highly obscured growth of $z > 7$ quasars *Astrophysical Journal Letter* **884**, L19 (2019).

Extended Data Tables

Extended Data Table 1| Multi-wavelength photometry of GNz7q

Observed λ [μm]	Flux density‡ [μJy]	Uncertainty [μJy]	Telescope	Instrument	reference
0.44	0.000	0.008	*HST*	ACS/F435W	This work (CHArGE)
0.61	-0.006	0.005	*HST*	ACS/F606W	”
0.78	0.005	0.007	*HST*	ACS/F775W	”
0.81	-0.011	0.006	*HST*	ACS/F814W	”
0.85	0.056	0.010	*HST*	ACS/F850LP	”
1.05	0.683	0.036	*HST*	WFC3/F105W	”
1.25	1.307	0.067	*HST*	WFC3/F125W	”
1.40	1.783	0.092	*HST*	WFC3/F140W	”
1.60	2.103	0.107	*HST*	WFC3/F160W	”
2.15	2.778	0.044	Subaru	MORICS/$K_{\rm s}$	Kajisawa et al. 2011
3.6	3.574	0.180	*Spitzer*	IRAC/ch1	This work (CHArGE)
4.5	3.907	0.197	*Spitzer*	IRAC/ch2	”
5.8	4.138	0.546	*Spitzer*	IRAC/ch3	”
8.0	4.553	0.471	*Spitzer*	IRAC/ch4	”
24	28.1	6.6	*Spitzer*	MIPS	Magnelli et al. 2011
100	<1050	350	*Herschel*	PACS	Liu et al. 2018
160	<2850	950	*Herschel*	PACS	”
250	$<17{,}100$	5,700	*Herschel*	SPIRE	Oliver et al. 2012
350	$<18{,}300$	6,100	*Herschel*	SPIRE	”
500	$<12{,}300$	4,100	*Herschel*	SPIRE	”
450	8,000	5,500	JCMT	SCUBA2	This work
850	1,800	390	JCMT	SCUBA2	Cowie et al. 2017
1,284	460	94†	NOEMA	Band 3	This work
3,276	24.6	6.9†	NOEMA	Band 1	This work
30,000	0.8	1.1	JVLA	X Band	Murphy et al. 2017
200,000	22.4	6.4	JVLA	L Band	Owen 2018

‡ The potential contributions from nearby objects are subtracted, or confirmed to be negligible (Section 5).

† The additional uncertainty of the absolute flux calibration is included by 20% and 10% at 1-mm and 3-mm band, respectively.

Extended Data Table 2| Measured and derived source properties

Parameter	Value	Description
R.A.	12:36:16.9195	Right Ascension (J2000) in *HST*
Decl.	62:12:32.127	Declination (J2000) in *HST*
$z_{\rm UV}$	7.23 ± 0.05	Redshift from *HST* grism spectrum
$z_{\rm [CII]}$	7.1899 ± 0.0005	Redshift from [C II] line
α_λ	0.1 ± 0.3	Rest-frame UV continuum slope
$L_{2,500}$	$(2.1 \pm 0.1) \times 10^{30}$ erg s^{-1} Hz^{-1}	Monochromatic optical luminosity at rest-frame 2,500 Å
$L'_{2,500}$	$(3.2 \pm 0.1) \times 10^{30}$ erg s^{-1} Hz^{-1}	Dust corrected $L_{2,500}$
$L_{\rm bol}$	$1.7 \pm 0.1 \times 10^{46}$ erg s^{-1}	AGN bolometric luminosity (rest-frame 1216Å–20 cm)
$A_{\rm V,\,qso}$	0.3 ± 0.1	Dust attenuation for the quasar component
$A_{\rm V,\,host}$	> 6	Dust attenuation for the host galaxy component
$L_{\rm X}$	$< 3.9 \times 10^{42}$ erg s^{-1}	Rest-frame X-ray (2–10 keV) luminosity
$L_{\rm 2keV}$	$< 5.1 \times 10^{24}$ erg s^{-1} Hz^{-1}	Monochromatic X-ray luminosity at rest-frame 2 keV
$\alpha_{\rm ox}$	< -2.23	Optical to X-ray spectral index
$L_{\rm IR}$	$(1.2 \pm 0.6) \times 10^{13}\ L_\odot$	Rest-frame IR (8–1,000 μm) luminosity
$L_{\rm IR,\,SF}$	$(1.1 \pm 0.5) \times 10^{13}\ L_\odot$	Rest-frame IR luminosity for the host galaxy component
$L_{\rm IR,\,AGN}$	$(1.0 \pm 0.3) \times 10^{12}\ L_\odot$	Rest-frame IR luminosity for the AGN component
$f_{\rm AGN}$	8 ± 5 %	AGN contribution to $L_{\rm IR}$
$T_{\rm d}$	80 ± 21 K	Peak dust temperature
$L_{\rm [CII]}$	$(1.1 \pm 0.3) \times 10^9\ L_\odot$	[C II] line luminosity
$L_{\rm CO(7-6)}$	$(1.3 \pm 0.7) \times 10^8\ L_\odot$	CO(7-6) line luminosity
FWHM$_{\rm [CII]}$	280 ± 40 km s^{-1}	FWHM of the [C II] line
FWHM$_{\rm CO}$	770 ± 230 km s^{-1}	FWHM of the CO(7-6) line
$L_{\rm CO(6-5)}$	$< 5.0 \times 10^7\ L_\odot$	CO(6-5) line luminosity ([C II] line width assumed)
$L_{\rm [CI]2-1}$	$< 7.9 \times 10^7\ L_\odot$	[C I](2-1) line luminosity ([C II] line width assumed)
SFR	$1,600 \pm 700\ M_\odot$ yr^{-1}	SFR of the host galaxy
$M_{\rm dust}$	$(1.6 \pm 1.1) \times 10^8\ M_\odot$	Dust mass of the host galaxy
$M_{\rm gas}$	$(2.0 \pm 1.2) \times 10^{10}\ M_\odot$	Gas mass of the host galaxy
$M_{\rm dyn}$	$(4.5 \pm 0.9) \times 10^{10}\ M_\odot$	Dynamical mass
$M_{\rm star}$	$(2.5 \pm 1.4) \times 10^{10}\ M_\odot$	Stellar mass of the host galaxy from $M_{\rm dyn} - M_{\rm gas}$
$q_{\rm IR}$	2.1 ± 0.3	IR/radio correlation
$\alpha_{\rm radio}$	$< -1.0 \pm 0.6$	Radio spectral index
$r_{\rm e,FIR}$	< 0.48 kpc	Effective radius of the rest-frame FIR continuum
$r_{\rm e,[CII]}$	1.4 ± 0.2 kpc	Effective radius of the [C II] line

Extended Data Figures

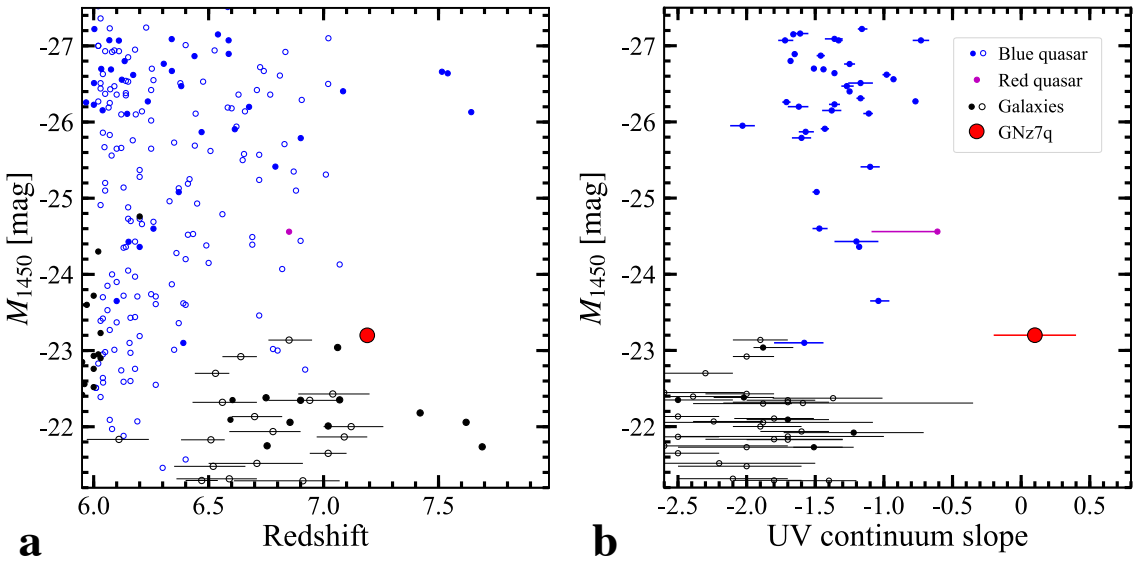

Extended Data Figure 1 | Rest-frame UV properties of GNz7q. The rest-frame 1450 Å luminosity as a function of redshift (**a**) and the UV continuum slope (**b**). GNz7q falls between the typical luminosity ranges of quasars and galaxies in the literature[2,6,48,49], where both faint quasars and luminous galaxies have been also identified[50–55,57,148]. GNz7q shows the reddest UV continuum slope among both galaxies and quasars at $z > 6$. The galaxies without spectroscopic redshifts and the quasars without a UV continuum slope measurement are displayed in the open symbols. The error bars denote the 1σ measurement uncertainty.

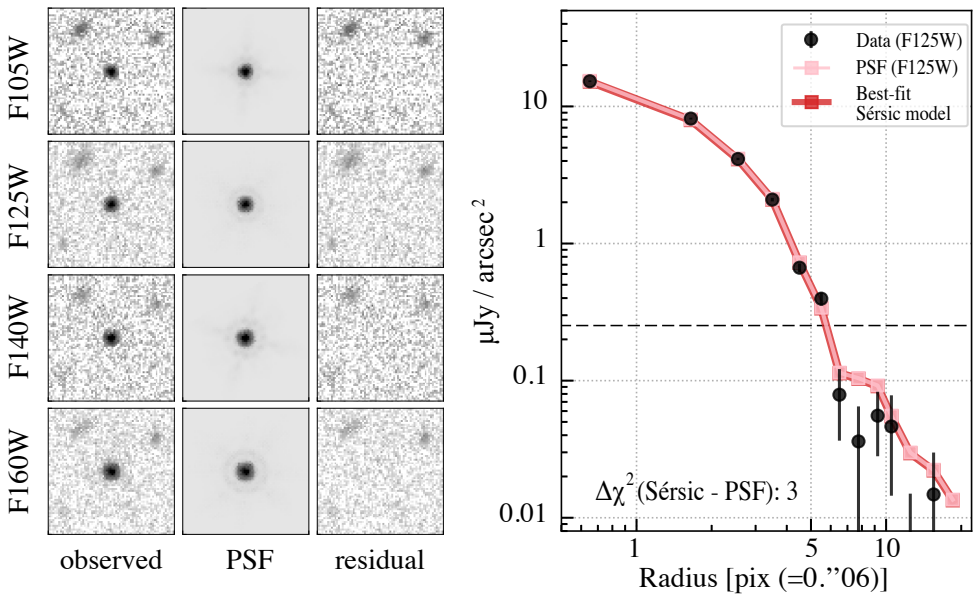

Extended Data Figure 2 | Point-source morphology of GNz7q. **a**, HST $4'' \times 4''$ cutout in the HST WFC3/IR filters of F105W, F125W, F140W, and F160W (left), instrumental point spread function (PSF) models[167] (centre), and PSF fit residuals (right). **b**, Radial profile for the rest-frame UV continuum of GNz7q observed in F125W. The black circles show the observed values, while the dark and light red squares and lines present the PSF and the best-fit Sérsic models (see Methods). The error bars denote the 68th percentile in each annulus, and the dotted line indicates the standard deviation of the pixel.

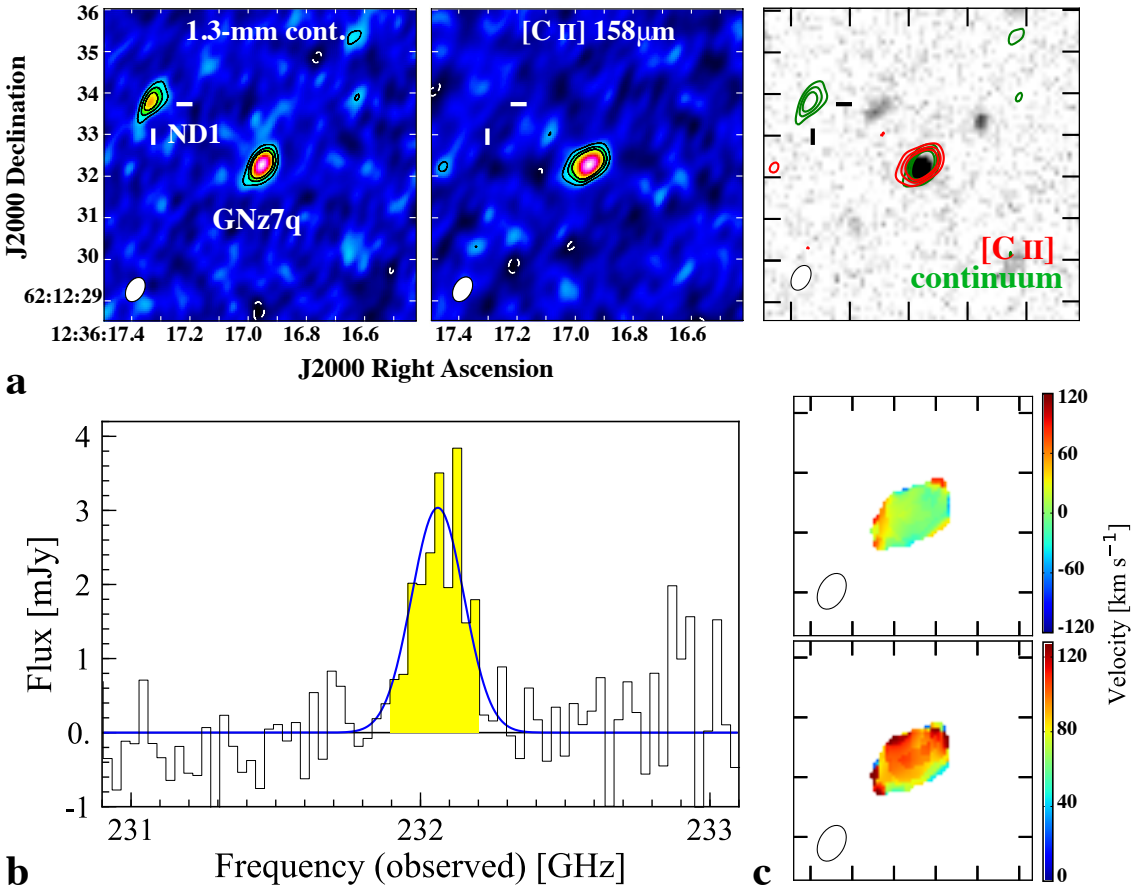

Extended Data Figure 3 | NOEMA 1-mm observation results. **a,** 1.3-mm continuum (left) and the velocity-integrated [C II] maps (middle) with the natural weighting. We identify a nearby continuum object with a $\sim 3''$ offset from GNz7q at the northern east part, dubbed "ND1". The intensity of the 1.3-mm continuum and the velocity integrated [C II] is shown in the right panel in green and red contours, respectively, overlaid on the HST/F160W $4'' \times 4''$ cutout. The solid contours are drawn at 3σ, 5σ, and 7σ levels, while the dashed white contours are drown at -3σ level. The NOEMA synthesized beam is presented at the left bottom. **b,** [C II] line spectrum within a $1.''0$ radius aperture. The blue curve is the best-fit Gaussian for the [C II] line. The yellow shaded indicates the velocity range of $[-200 : +200]$ km s^{-1} used for the velocity-integrated map in panel **a**. **c,** [C II] line kinematics. The top and bottom panel present the velocity-weighted and the velocity-dispersion maps ($4'' \times 4''$), respectively.

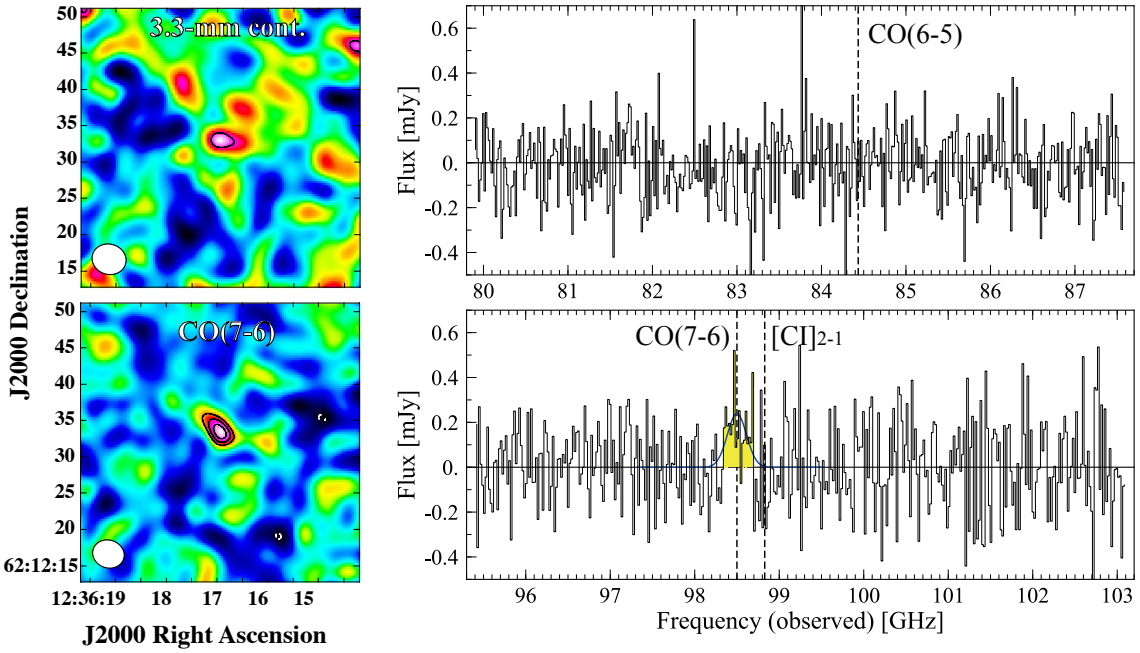

Extended Data Figure 4 | NOEMA 3-mm observation results. **Left,** 3.3-mm continuum (top) and the velocity-integrated CO(7-6) maps with the natural weighting. The black (white) contours are drown at 3σ, 4σ, and 5σ (-3σ). **Right,** NOEMA 3-mm band spectrum for LSB (top) and USB (bottom) with a $2.''0$ radius aperture. The dashed vertical line indicates the observed frequency of the expected far-IR lines based on the source redshift of $z = 7.1899$ determined by the [C II] line. The blue curve is the best-fit Gaussian for the CO(7-6) line. The yellow shade indicates the velocity range used for the velocity-integrated map in the left panel.

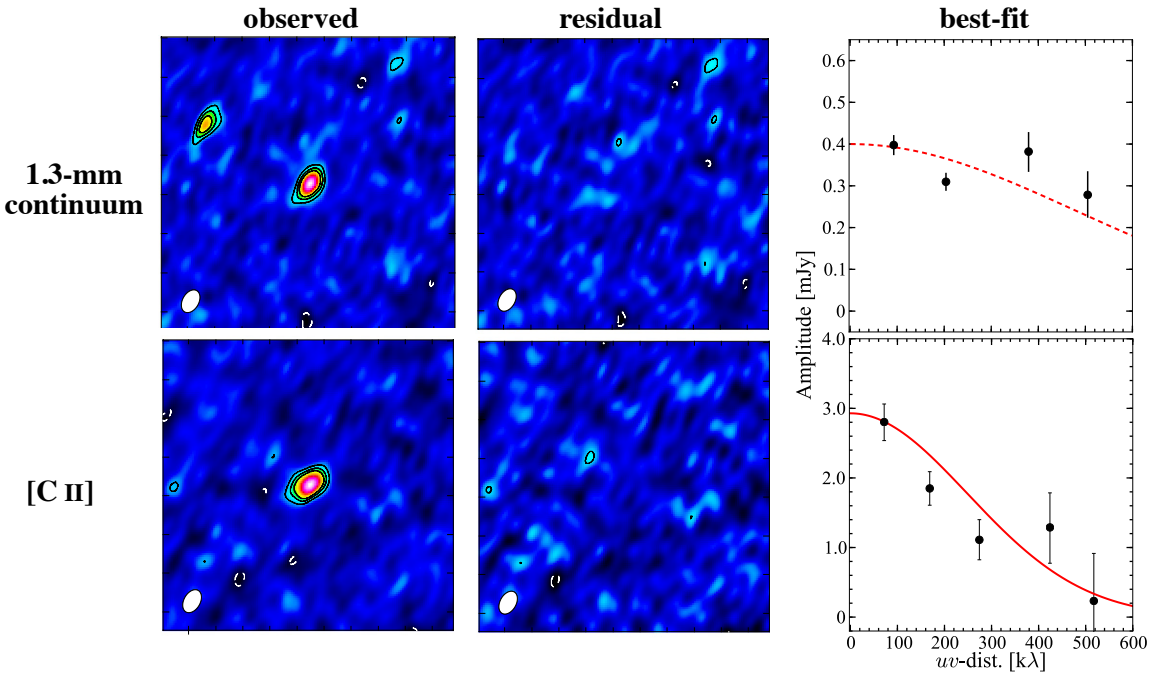

Extended Data Figure 5 | 1.3-mm continuum (top) and [C II] (bottom) size measurement results. **Left,** Observed map, which is the same as Extended Fig. 3a. **Middle,** Residual map by subtracting the best-fit model visibility obtained with UVMODELFIT. For the dust continuum, we subtract the best-fit model visibility by fixing the major-axis effective radius as the upper limit value of $r_{\rm e,FIR} = 0.48$ kpc. The visibility of ND1 is subtracted by assuming its profile as a point source before running UVMODELFIT. **Right,** Amplitude as a function of uv distance. The black circles shows the observed visibility. The error bars show the standard error of the mean in each uv distance bin. The red curve denotes the best-fit uv model for the [C II] line, while the red dashed curve for the dust continuum indicates the uv model with the upper limit size.

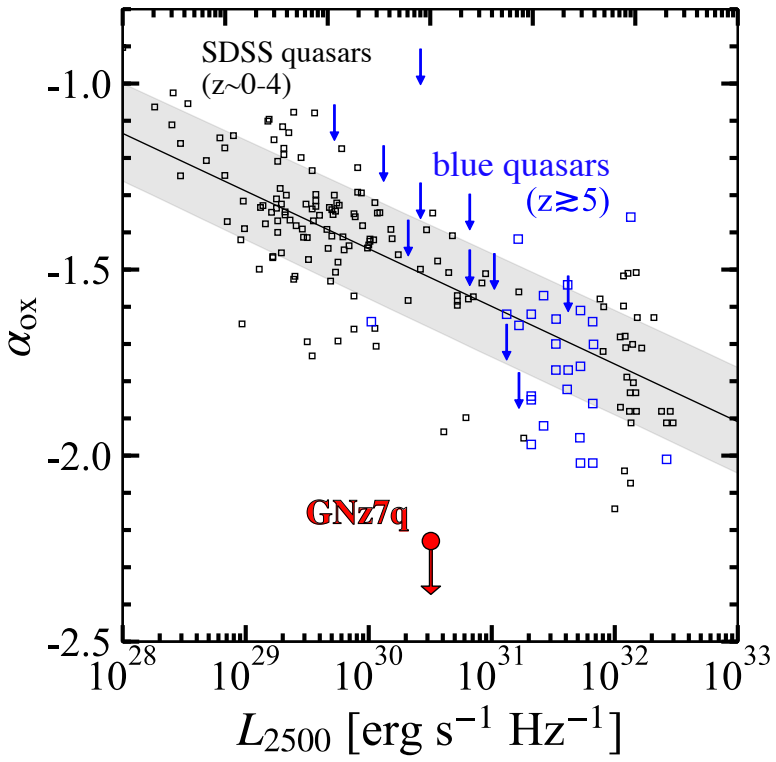

Extended Data Figure 6 | Optical luminosity vs. α_{ox} correlation. The black and blue squares denote SDSS quasars[18,81,168] at z ∼0–4 and blue quasars[77,82,85] at $z > 5$ respectively, taken from the literature. The arrows present the upper limits. The black line represents the best-fit relation based on 1544 quasars taken from the literature[77]. The gray shaded region denotes the 68th percentile derivation, evaluated by propagating the 1σ uncertainties of the parameters that define the best-fit relation. The α_{ox} upper limit of GNz7q (99% confidence level) is estimated after the extinction correction and deviated from the best-fit relation by more than 5σ.

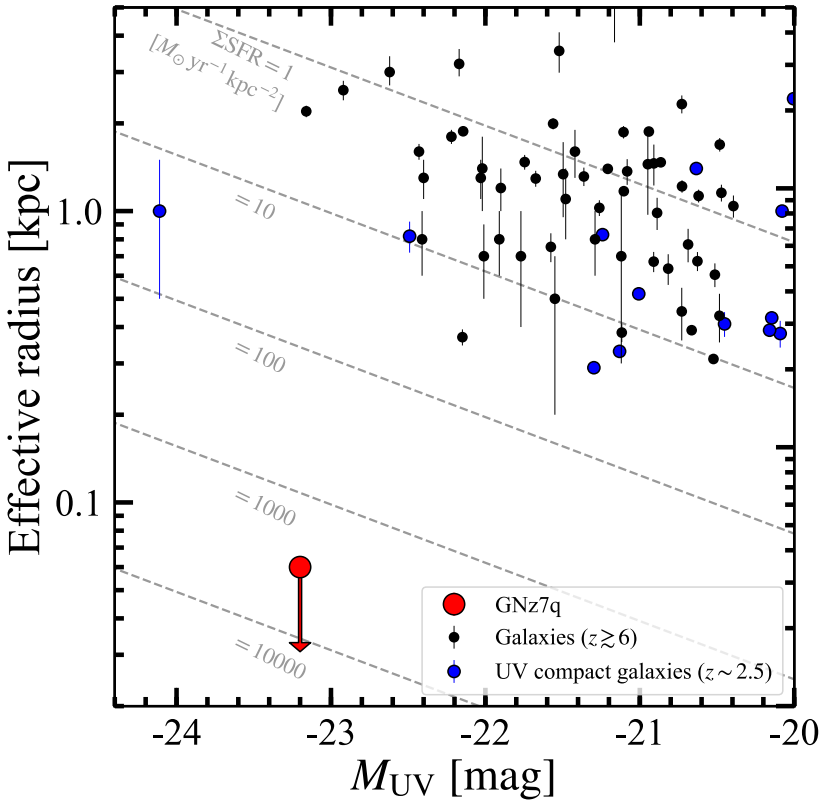

Extended Data Figure 7 | Rest-frame UV size and luminosity relation. The black and blue circles show the rest-frame UV size measurements in the literature for galaxies[50,91] at $z > 5.5$ and for compact galaxies reported at $z \sim$ 2–3, respectively[16,90], but no objects similarly compact and luminous to GNz7q have been identified. The error bar denotes the 1σ measurement uncertainty, and the sources whose errors exceed the measurements are not presented. The dashed line indicates the SFR surface density ($\Sigma_{\rm SFR}$) by converting the UV luminosity to SFR[112]. If the compact UV emission in GNz7q is attributed to the star-forming activity, $\Sigma_{\rm SFR}$ reaches $\gtrsim$ 5,000 $M_\odot$ yr^{-1} kpc^{-2}. Note that the UV luminosity is the observed value, and thus $\Sigma_{\rm SFR}$ of GNz7q after dust correction will be more extreme in the star-forming scenario.

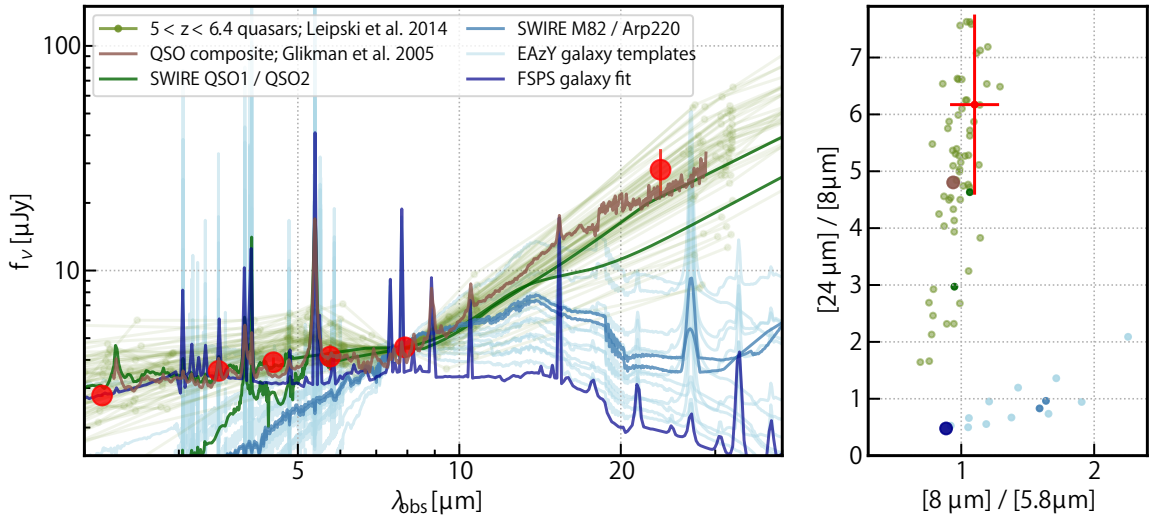

Extended Data Figure 8 | NIR–MIR SED of GNz7q. *Left:* Observed-frame SED of GNz7q traced by the *Spitzer* IRAC and MIPS 24 μm bands. The dark blue curve is the best-fit galaxy template (stellar continuum plus nebular emission from ionized gas in HII regions) constrained at $\lambda_{\rm obs} < 10\,\mu$m. The thin light blue curves are additional galaxy templates that largely span the galaxy color space at lower redshifts[94], and the thicker light blue curves are templates of nearby dusty starbursts M82 and Arp220[95]. The thick green curves are templates of Type 1 and 2 quasars[95], and the brown curve is a composite spectrum of nearby quasars[96]. The light green curves show the broad-band SEDs of high-redshift quasars at $5 < z < 6.4$[97] interpolated to the redshift of GNz7q. Other than the galaxy fit, all SEDs and templates are normalized to the observed 8 μm flux density of GNz7q. *Right:* Observed-frame MIR flux ratio diagram for the flux densities at 5.8 μm, 8 μm, and 24 μm as observed for GNz7q and integrated from the SEDs displayed in the left panel. No templates from stars and star formation alone (blue curves and points) can reproduce the flux enhancement at 24 μm (rest-frame 3 μm) of GNz7q, which is fully consistent with the colors of luminous quasars at both low and high redshifts and likely arises from hot dust associated with an active nucleus. The error bars are obtained by propagating the 1σ measurement uncertainty of each photometry.

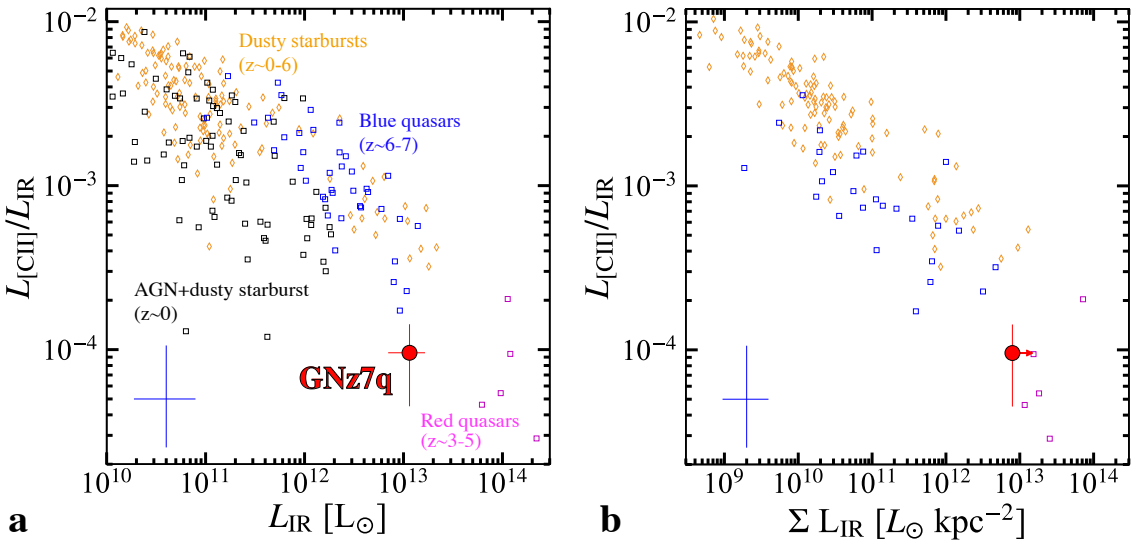

Extended Data Figure 9 | $L_{[CII]}$ and L_{IR} properties compared with other populations. We show $L_{[CII]}/L_{IR}$ as a function of L_{IR} (**a**) and ΣL_{IR} (**b**). For comparison, we also show observational results of local composite systems of AGN and starburst (black square), dusty starbursts at z ~0–7 (orange diamond), blue quasars at z ~6–7 (blue square), and red quasars at z ~3–5 (magenta square) taken from the literature[6,43,49,118,123,129,134,135,169]. GNz7q is at the extreme end of the relationship painted by known starbursts and quasars. The L_{IR} values of the blue quasars are calculated by assuming the single modified blackbody ($T_d = 47$ K; $\beta_d = 1.6$), where the blue bar at the bottom left of the left panel shows a potential error scale with a change of T_d by ± 10 K from the assumption. For GNz7q, the error bar is obtained by propagating the 1σ uncertainties of $L_{[CII]}$ and L_{IR}.

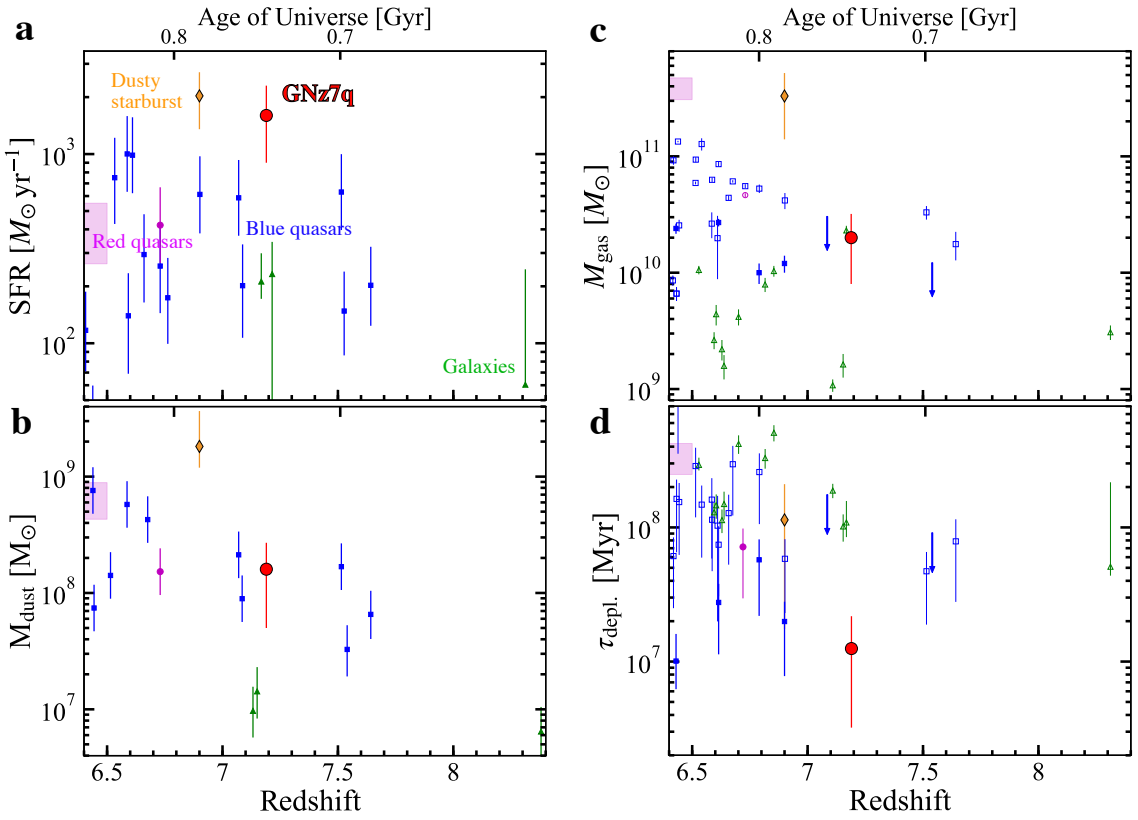

Extended Data Figure 10 | Host galaxy properties compared with other populations at $z > 6$. a–d, We show (a) SFR, (b) $M_{\rm dust}$, (c) $M_{\rm gas}$, (d) and $\tau_{\rm depl.}$ as a function of redshift. For comparison, we also show other galaxy populations with spectroscopic redshifts: blue quasars (blue square), red quasars (magenta circle and shaded region), Lyman-break galaxies (green triangle), and a dusty starburst galaxy (orange circle) that are taken from the literature[6,25,29,43,49,86,118,124,137,143]. The magenta shade represents the 68th percentile of the host galaxy properties of the super-Eddington accretion red quasar, W2246-0526, at $z = 4.6$[43,141]. The host galaxy of GNz7q show the most vigorously star-forming system at $z > 7$ with the large gas reservoir. The filled and open symbols in panel (c) denote $M_{\rm gas}$ estimates from CO and [C II] lines, respectively. The error bars of SFR and $M_{\rm dust}$ are estimated by propagating the 1σ measurement uncertainty and a 0.2-dex uncertainty of the $T_{\rm d}$ assumption, when they are derived from a single submm-mm band (Section 8). The error bars of $M_{\rm gas}$ and $\tau_{\rm depl.}$ are estimated with the 1σ measurement uncertainty and the propagation from both SFR and $M_{\rm gas}$ uncertainties, respectively. For all populations, the different assumptions of the initial mass function and the dust opacity coefficient among the literature are corrected.

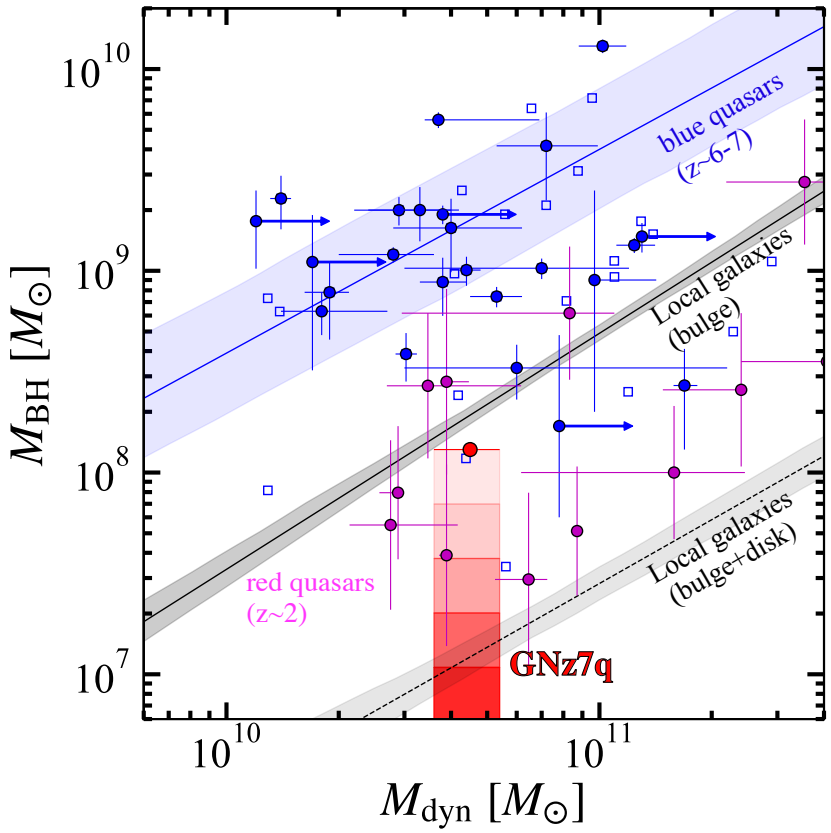

Extended Data Figure 11 | $M_{\rm dyn}$ **and** $M_{\rm BH}$ **relation**. The colour scale and the vertical range of red-shade regions correspond to those of Fig. 3. The red circle and the red-shade regions show the potential $M_{\rm BH}$ range of GNz7q suggested by its faint $L_{\rm bol}$ and extremely faint X-ray property, respectively. The horizontal range of the red-shade regions indicates the 68th percentile of the $M_{\rm dyn}$ estimate from the [C II] line. For comparison, we also present $M_{\rm BH}$ and $M_{\rm dyn}$ (or $M_{\rm star}$) estimates for blue quasars at $z \sim$ 6–7 (blue squares)[48,128,129,146–148,150,151] and red quasars at $z \sim 2$ (magenta circles)[133]. The error bars denote the 1σ uncertainties taken from the literature. The $M_{\rm dyn}$ values from the kinematic analysis based on the 3D modeling are shown in the filled blue squares with the 1σ error bars[146,147]. The $M_{\rm dyn}$ measurements based on the rotation-disk assumption in the literature are shown by the open blue squares. The best-fit relation for the filled blue squares is shown by the blue line[146]. The black solid line represents the best-fit relation between the bulge mass and $M_{\rm BH}$ among local quiescent galaxies[152]. The black dashed line denotes the best-fit relation between the stellar mass of the entire system and $M_{\rm BH}$ among local AGNs[153]. The shaded regions present the 1σ confidence level for the best-fit relations.